EES Solar

PAPER

View Article Online
View Journal | View Issue

Cite this: *EES Sol.*, 2025, **1**, 796

Effect of buffer layers on the photovoltaic performance of bifacial transparent perovskite solar cells under different albedo conditions†

Farhan Yousuf, [a] Ming-Xun Jiang,[a] Chen-Fu Lin,[a] Ming-Hsien Li, [b] Chih-Wei Chu, [cd] Tzung-Fang Guo[acdf] and Peter Chen [*adef]

Perovskite solar cells (PSCs) have made significant advancements, achieving a power conversion efficiency of up to 27%. PSCs are easy to manufacture and cost-effective, making them highly attractive for commercial applications. This study focuses on bifacial transparent PSCs, which utilize transparent electrodes instead of metal electrodes, allowing light absorption from both sides and thereby enhancing energy utilization efficiency. The introduction of buffer layers is aimed at protecting the perovskite absorption layer and organic transport layer from damage during the sputtering process of transparent conductive oxides (TCOs). This research evaluates the effectiveness of three buffer layer preparation methods, soft sputtering deposition, spin coating, and atomic layer deposition (ALD), for bifacial PSCs under various illumination conditions. The results indicated that the bifacial devices with ALD-prepared buffer layers exhibit the best performance under specific albedo conditions, with a front-side illuminated efficiency of 16.2% and a rear-side illuminated efficiency of 15.4% under AM 1.5 G illumination (1 sun), resulting in a bifacial factor of 0.95. A MA-free bifacial PSC with a p-i-n architecture of composition $FA_{0.78}Cs_{0.22}Pb(I_{0.85}Br_{0.15})_3$ delivers a front-side (glass-side) illuminated efficiency of 19.7% and a rear-side (IZO-side) illuminated efficiency of 18.0% under AM 1.5 G illumination (1 sun). The device exhibited excellent bifacial characteristics, achieving a bifacial factor of 0.91, with a frontside short-circuit current density (J_{sc}) of 22.8 mA cm^{-2} and a rear-side J_{sc} of 20.8 mA cm^{-2}. As the albedo light intensity increases, the bifacial device achieves a significant gain in output power, highlighting the potential of bifacial transparent PSCs in environmental light harvesting scenarios. These results highlight the potential of MA-free perovskite bifacial solar cells as high-efficiency and stable energy conversion candidates, paving the way for further optimization in tandem and large-area photovoltaic applications.

Received 30th March 2025
Accepted 24th July 2025

DOI: 10.1039/d5el00045a

rsc.li/EESSolar

Broader context

The growing demand for sustainable energy solutions has intensified research into high-performance photovoltaic technologies, particularly bifacial solar cells. Enhancing efficiency and stability while maintaining cost-effectiveness remains a major challenge in the commercialization of these devices. In this work, we investigate the impact of buffer layers on the photovoltaic performance of bifacial perovskite solar cells, comparing MA-free perovskite and triple-cation perovskite materials. Our findings reveal that the MA-free perovskite devices achieved a superior power output of 33 mW cm^{-2} with a bifacial factor of 90%, while the triple-cation perovskite devices demonstrated bifacial performance with a power output of 29 mW cm^{-2} with a bifacial factor of 95% under 1 sun illumination intensity from each side. By systematically investigating different buffer layer materials and their impact on charge transport, interface recombination, and optical management, our findings offer valuable insights for advancing the next generation of photovoltaic devices. By improving energy harvesting from both sides, our research contributes to the ongoing pursuit of high-efficiency, cost-effective solar solutions that maximize power output in real-world applications. This study aligns with the global aim for clean energy solutions and contributes to the broader effort of making perovskite photovoltaics commercially viable.

[a]*Department of Photonics, National Cheng Kung University, Tainan 70101, Taiwan. E-mail: petercyc@ncku.edu.tw*

[b]*Department of Electro-Optical Engineering, National Formosa University, Yunlin 63201, Taiwan*

[c]*Research Center for Applied Sciences (RCAS), Academia Sinica, Taipei 11529, Taiwan*

[d]*Research Center for Critical Issues (RCCI), Academia Sinica, Tainan, 711010, Taiwan*

[e]*Hierarchical Green-Energy Materials (Hi-GEM) Research Center, National Cheng Kung University, Tainan 70101, Taiwan*

[f]*Program on Key Materials, Academy of Innovative Semiconductor and Sustainable Manufacturing, National Cheng Kung University, Tainan 70101, Taiwan*

† Electronic supplementary information (ESI) available. See DOI: https://doi.org/10.1039/d5el00045a

1. Introduction

The introduction of bifacial illuminated solar cells offers new potential and opportunities for advancing photovoltaic (PV) technology.[1–3] Compared with traditional single-sided illuminated devices, bifacial illuminated solar cells provide higher power output and lower cost per unit area without significantly increasing manufacturing costs.[4–6] This may lead to a lower levelized cost of energy (LCOE) in the long run compared with their single-side illuminated counterparts. However, achieving

efficient bifacial illuminated designs in inorganic thin-film solar cells faces challenges such as short carrier lifetimes and high rear-side carrier recombination rates.[3] Among the PV technologies, metal halide perovskite solar cells (PSCs) have garnered significant interest from academia and industry due to their rapidly increasing power conversion efficiency (PCE), excellent optoelectronic properties, unique device characteristics and ease of production. Over the past decade, PSCs have rapidly developed and can now compete with other mature PV technologies. Recently, PSCs have achieved a remarkable PCE as high as 27%,[7–9] presenting a wonderful opportunity for high-performance bifacial illuminated thin-film solar cells. Moreover, recent innovations in device architecture, such as the incorporation of passivation layers and optimization of the absorber layer, have further enhanced the stability and efficiency of PSCs.[10–12] The integration of advanced encapsulation techniques also plays a critical role in extending the operational lifespan of PSCs, making them more viable for commercial applications. The continuous improvement in PSC technology, combined with the inherent advantages of bifacial designs, will pave the way for the next generation of highly efficient, cost-effective, low LCOE and durable PV solutions. Moreover, it is expected that bifacial illuminated PSCs will play a pivotal role in the global transition towards renewable energy sources. For the fabrication of bifacial illuminated PSCs, the use of transparent conductive oxide (TCO) electrodes can prevent halide ion corrosion of the electrodes,[13–16] thereby mitigating a significant instability issue.

In this article, we investigated the formation of a transparent window layer for bifacial illuminated PSCs by sputtering transparent conductive electrodes on top of the perovskite. To prevent sputtering damage to the perovskite layer, various methods such as soft-landing sputtering, spin coating, and atomic layer deposition (ALD) were employed to prepare buffer layers. Among these, the ALD buffer layer minimized sputtering damage and maintained a PCE of around 16% for bifacial transparent cells with an anti-reflection coating (ARC). Additionally, bifacial illumination simulations were conducted under different scenarios such as sunny (1 sun), cloudy (0.6 sun), and rainy (0.2 sun) conditions to understand the photovoltaic characteristics of bifacial solar cells under various albedo conditions. Under ample sunlight conditions (1 sun), when the albedo is less than 0.4 sun, only bifacial devices with ALD-deposited films as buffer layers and anti-reflection layers achieve higher power output per unit area than opaque devices. Under simulated cloudy conditions (0.6 sun), bifacial devices with ALD buffer layers require an albedo of less than 0.1 sun (with an ARC) and 0.2 sun (without an ARC) to achieve superior power output compared to opaque devices, while the bifacial devices with spin-coated buffer layers need to increase the albedo to 0.3 sun to surpass the power output of opaque devices. Finally, under simulated indoor conditions (0.2 sun), regardless of the buffer layer preparation method, bifacial devices only need an albedo of 0.2 sun to achieve higher power output than opaque devices. In conclusion, it is indicated that the bifacial illuminated PSCs with proper design can harvest more energy in different scenarios.

2. Results and discussion

In bifacial devices, it is necessary to replace the metal electrode used in monofacial devices with a transparent electrode. The structure of the monofacial device used in this study is FTO/Me-4PACz/perovskite/C_{60}/BCP/Ag. In the bifacial device, the BCP/Ag in the monofacial device is replaced with a buffer and an indium zinc oxide (IZO) transparent rear electrode. A metal finger electrode is then evaporated to surround the active area, further enhancing the carrier collection ability of the transparent back electrode. The structure of the bifacial device is FTO/Me-4PACz/perovskite/C_{60}/(w/o or w/ buffer layer)/IZO/Ag grid, as illustrated in Fig. 1(a). The impact of plasma during sputtering on bifacial devices with and without a buffer layer is investigated. The cross-sectional SEM image of the bifacial device is shown in Fig. 1(b).

2.1 Impact of plasma on buffer-less bifacial devices during IZO film sputtering

During the magnetron sputtering process, there are different electronegative elements involved, including negative ions and electrons. In the growth of TCO films, most of these negative ions originate from O^- on the surface of the oxide target and the other are formed through reactive sputtering. The energy of the O^- ion bombardment is equal to the target voltage, which often exceeds 100 eV. Such high-energy bombardment can cause significant energetic damage to the organic transport layers and the underlying perovskite light-absorbing layer.[17–19] In order to understand the impact of sputtering damage on the device without a buffer layer, the IZO film with optimized parameters (sputtering power = 100 W; deposition time = 40 min; substrate without heating) was directly deposited on the electron transport layer (C_{60}) and the device performance is shown in Fig. 2. As a result, the *J*–*V* curve of the device shows a linear resistive behavior under AM 1.5 G illumination, suggesting direct contact between FTO and IZO due to bombardment damage to the C_{60} and perovskite layers.

To reduce the bombardment damage on the surface of C_{60} during the IZO film deposition, we studied the IZO deposition using a 2-step process. In the first stage, a soft deposition approach was employed with the sputtering power reduced to 10 W, which is the minimum power capable of plasma generation and the V_{bias} ranging from 70 to 75 V with a working pressure of 7 mTorr. Additionally, a trace amount of oxygen (Ar/O_2 = 0.33%) was introduced during the IZO film deposition to enhance the optical properties of the IZO film and decrease the

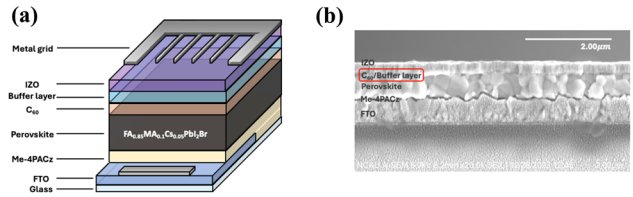

Fig. 1 Bifacial devices: (a) illustration and (b) cross-sectional SEM image.

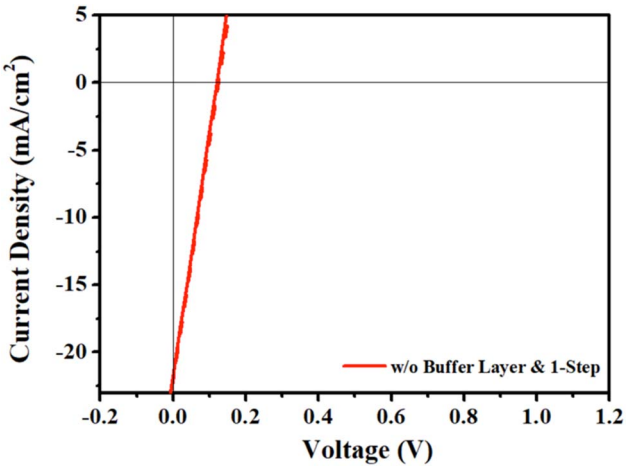

Fig. 2 The *J*–*V* curves of the bifacial device where the IZO film is directly deposited on the C_{60} layer without any buffer layer.

kinetic energy of deposited IZO particles in the first-stage soft deposition.[20] The second stage utilized the optimized sputtering parameters (sputtering power = 100 W) to obtain high transparency and good electric conductivity of the IZO film. Bifacial devices prepared using this 2-step deposition process, without a buffer layer between the C_{60} layer and IZO film, demonstrated a significantly improved diode behavior. The *J*–*V* curves of bifacial devices with different deposition times in the first step, under AM 1.5 G illumination, are shown in Fig. 3.

It is clear that the soft-landing deposition process transformed the *J*–*V* curves of devices from a linear shape (using 1-step IZO deposition, Fig. 2) to an S-shape (2-step IZO deposition, Fig. 3) characteristic under reduced target power and bias voltage. Specifically, the device under front illumination achieves a peak PCE of 8.2% with a 20-minute soft deposition time in the first stage. The longer soft deposition time results in a thicker soft-deposited IZO film and reduces bombardment

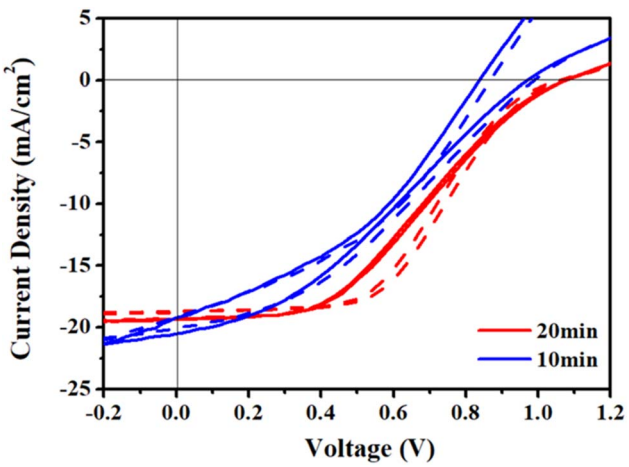

Fig. 3 The *J*–*V* curves (solid: forward scan and dashed: reverse scan) for bifacial devices fabricated with different soft deposition times of IZO in the first step of the 2-step IZO process under AM 1.5 G illumination.

damage from subsequent high-power IZO film deposition. Deposition beyond 20 minutes (*e.g.*, 30 minutes) resulted in increased series resistance and degraded transparency, limiting overall efficiency. Thus, 10 and 20 minutes were selected to achieve an optimal trade-off (Fig. S1†). The S-shape *J*–*V* behavior under high bias voltage suggested that plasma still damages the C_{60}/IZO interface even under such soft sputtering conditions. This damage induces defects within the C_{60}/IZO interface and may introduce energy barriers, such as Schottky barriers, at the interface.[21,22]

2.2 Using a sputtering process to prepare a SnO_2 (tin oxide) buffer layer

To understand whether such a sputtering approach is material dependent, we further utilized a soft deposition sputtering process of a SnO_2 film as the buffer layer in the bifacial device. SnO_2, with its wide bandgap, exhibits excellent optical properties and high material stability, making it the most commonly used buffer layer material for bifacial devices.[23] During the sputtering process, the same trace amount of oxygen (Ar/O_2 = 0.33%) is introduced to inhibit the plasma damage. The SnO_2 target requires a minimum power of 20 W to initiate plasma for SnO_2 deposition, which is higher than that used for the first step of soft IZO deposition (10 W). As a result, the power of the first step SnO_2 layer is 20 W with the V_{bias} ranging from 90 to 95 V with a working pressure of 7 mTorr. Using these sputtering process parameters, SnO_2 buffer layers with thicknesses of 5 nm, 10 nm, and 15 nm were deposited for the bifacial devices. The PV parameters and *J*–*V* curves of bifacial devices with different SnO_2 thicknesses under front illumination (from FTO substrate) are shown in Fig. 4 and Table 1.

The 5 nm SnO_2 buffer layer exhibits lower buffering capability compared to the 10 nm and 15 nm SnO_2 buffer layers. Consequently, during subsequent high-power deposition of IZO thin films, greater plasma damage occurs at the C_{60}/SnO_2 interface. This results in more severe carrier recombination at the interface, leading to an overall V_{oc} of only 0.43 V and a fill factor (FF) of 31.74% in the bifacial device with the 5 nm SnO_2 buffer layer. In contrast, thicker SnO_2 layers demonstrate better buffering capabilities. Devices with thicker SnO_2 layers achieve V_{oc} values exceeding 0.80 V and FF values above 45%. Among these, the 10 nm thickness shows the optimal performance with a PCE of 8.1%. However, it is indicated that the device performance with the SnO_2 buffer layer is slightly lower than that with 2-step IZO deposition due to the V_{bias} of the sputtering SnO_2 layer being approximately 20 V higher than that of the 2-step IZO devices, as mentioned in Section 2.1.

To further reduce bombardment damage during sputtering, the working pressure of SnO_2 film deposition was increased to 20 mTorr. As the working pressure increases, the shorter mean free path would lead to more collisions between SnO_2 particles and facilitate thermalization of the sputtered species to the mean kinetic energy of the surrounding gas atoms through energy transfer. Another effect under high working pressure is that scattering of the sputtered particles broadens their distribution of incident angles at the substrate, which might decrease

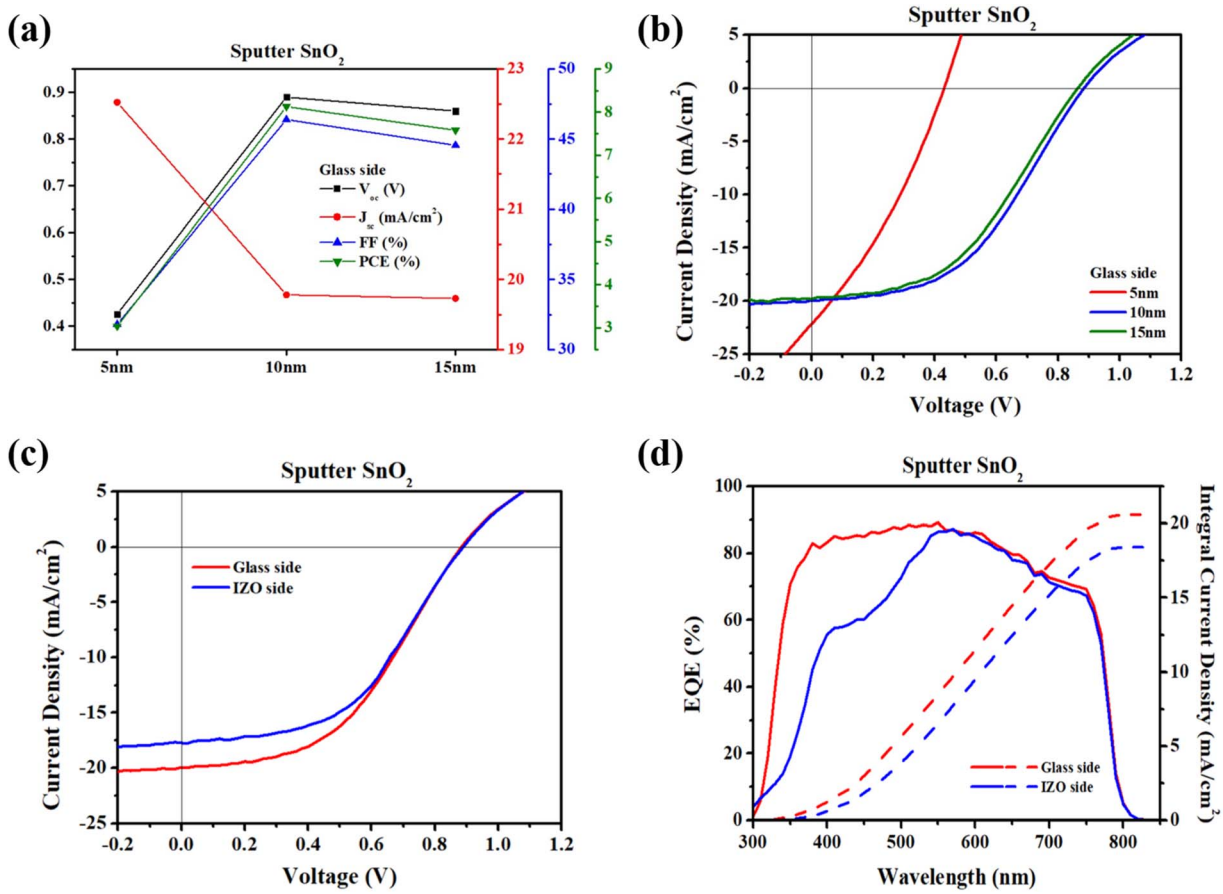

Fig. 4 (a) PV parameters and (b) *J*–*V* curves of the bifacial devices with different sputtered-buffer SnO_2 thicknesses under AM 1.5 G illumination through the FTO substrate. (c) *J*–*V* curves and (d) EQE spectra for 10 nm SnO_2 devices under front and rear illumination.

Table 1 Photovoltaic characteristics under front side illumination at various SnO_2 thicknesses

Thickness of SnO_2	V_{oc} (V)	J_{sc} (mA cm^{-2})	FF (%)	PCE (%)
5 nm	0.43	22.2	31.7	3.0
10 nm	0.88	20.0	46.1	8.1
15 nm	0.86	19.7	45.0	7.7

the penetration depth or impact on the deposited film. Under the high working pressure condition of 20 mTorr, the bifacial devices with 5 nm, 10 nm, and 15 nm SnO_2 buffer layers were fabricated and their device performances were measured. Excessively high pressure can accelerate thermal equilibration among deposited particles. Moreover, the deposited particles may reach the substrate without sufficient kinetic energy, shifting the film microstructure from the bombardment enhanced compact zone T to the porous zone structure. This scenario inhibits the device performance due to poor film quality, which impacts carrier transport and optical properties.[24] Therefore, maintaining appropriate working pressure is crucial for ensuring film quality and device performance. It can be observed that the efficiency of bifacial devices under front and rear illumination does not improve under high working pressure, as seen in Fig. 5.

2.3 To prepare a PEIE (polyethyleneimine ethoxylated) buffer layer using spin-coating

Even with adjustments of IZO sputtering parameters (Section 2.1) and changes in the material for soft deposition in the first stage (Section 2.2), effectively reducing plasma-induced damage during sputtering remains challenging due to inherent physical limitations. Therefore, we further investigated the process by introducing a spin-coated buffer layer for subsequent IZO deposition. Considering the buffer layer's requirement for excellent optical properties, this study utilizes polyethyleneimine ethoxylated (PEIE) as the material for spin coating the buffer layer.[25] Compared to other organic materials used for buffer layers, PEIE exhibits lower absorption in the 300 nm to 800 nm wavelength range, which is the main absorption band of perovskite. This characteristic minimizes optical losses for the bifacial-illuminated PSCs under back illumination conditions from the TCO layer.

Experimentally, we employ 2-propanol (IPA) to dilute a 37 wt% PEIE solution and compare different mass percentages of PEIE solutions. Here, 0 wt% PEIE denotes devices without a PEIE buffer layer, deposited with a 2-step IZO process

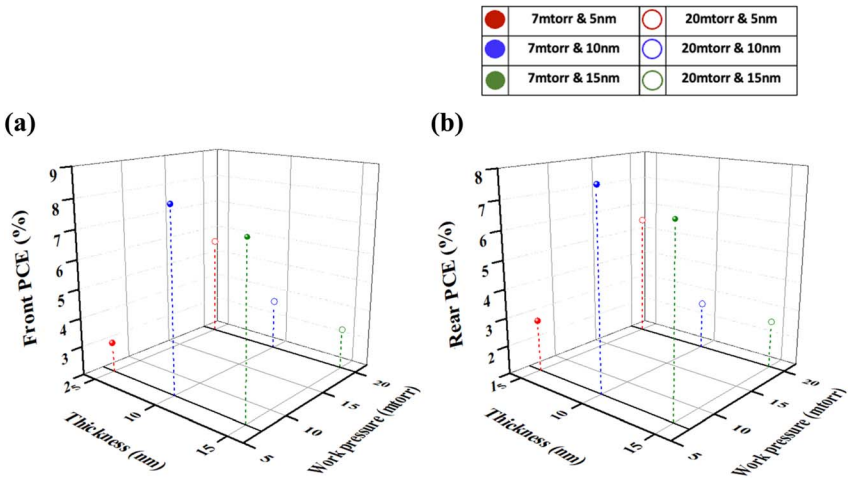

Fig. 5 For bifacial devices with sputtered buffer layers, measured under AM 1.5 G 1 sun illumination, the performance with different SnO_2 thicknesses and working pressures: (a) front-side efficiency and (b) rear-side efficiency.

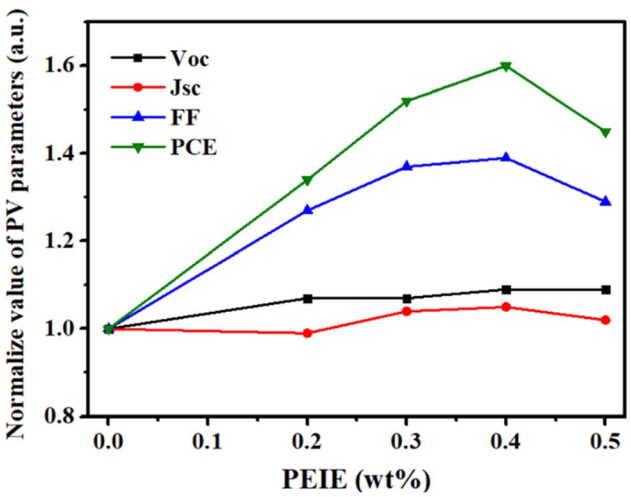

Fig. 6 Normalized PV parameters of bifacial devices with different PEIE concentrations under front-side 1 sun illumination.

for the bifacial cells. The PV parameters of the bifacial cells using various weight percents of PEIE are normalized to that of the device without buffer (0 wt% PEIE). The effect of PEIE concentration on the impact of PV characteristics is illustrated in Fig. 6. Table 2 shows the detailed photovoltaic characteristics of bifacial devices under front illumination for different PEIE concentrations.

Table 2 Photovoltaic characteristics of bifacial devices with different PEIE concentrations as buffer layers under front illumination

PEIE concentration (wt%)	V_{oc} (V)	J_{sc} (mA cm^{-2})	FF (%)	PCE (%)
0	0.90	18.1	51.0	8.3
0.2	0.96	18.0	64.5	11.2
0.3	0.96	18.9	69.7	12.7
0.4	0.98	19.1	71.2	13.3
0.5	0.98	18.4	66.8	12.0

In bifacial devices with 2-step IZO film deposition, incorporating PEIE as a buffer layer increased V_{oc} from 0.90 V to 0.96–0.98 V. This indicated that PEIE is effective at reducing the bombardment damage at the PEIE/IZO interface. The photovoltaic parameters of J_{sc} and FF both increase with increasing PEIE concentration. The optimal device performance was obtained at a PEIE concentration of 0.4 wt%, achieving a PCE of 13.3% under front illumination. The PV performance of the bifacial device with 0.4 wt% PEIE under front and rear illumination is shown in Fig. 7. The front-side and rear-side illuminated efficiency could reach 13.3% and 11.7%, giving a bifacial factor (defined by the ratio of rear-side illuminated efficiency to front-side illuminated efficiency) of 0.88 for the bifacial device. Table 3 shows the detailed photovoltaic characteristics of bifacial devices with 0.4 wt% PEIE under front and rear illumination. Compared to the device without a buffer layer, this represents an efficiency improvement of approximately 50%. However, as the concentration exceeded 0.5 wt%, the device performance began to decline due to the increased series resistance, which reduced the FF with such excessively high PEIE buffer layer concentration.

2.4 To prepare a SnO_2 buffer layer using atomic layer deposition (ALD)

To compare with the most commonly used materials and process for forming a buffer layer on top of perovskite, ALD was employed to prepare an SnO_2 buffer layer coupled with a 2-step IZO process. This was done to minimize plasma bombardment due to the high film compactness and conformality of ALD-deposited SnO_2 on the perovskite layer.[26–29] However, a lower PCE of 13.1% was achieved for the device with 10 nm ALD SnO_2, indicating no significant enhancement in PV performance compared to devices with a spin-coated PEIE buffer layer. Although the superior film quality of the oxide film prepared by ALD effectively minimizes the bombardment damage from the IZO film, the subsequent deposition of a 2-step IZO process on top of this ALD-prepared buffer layer, especially the soft-landing

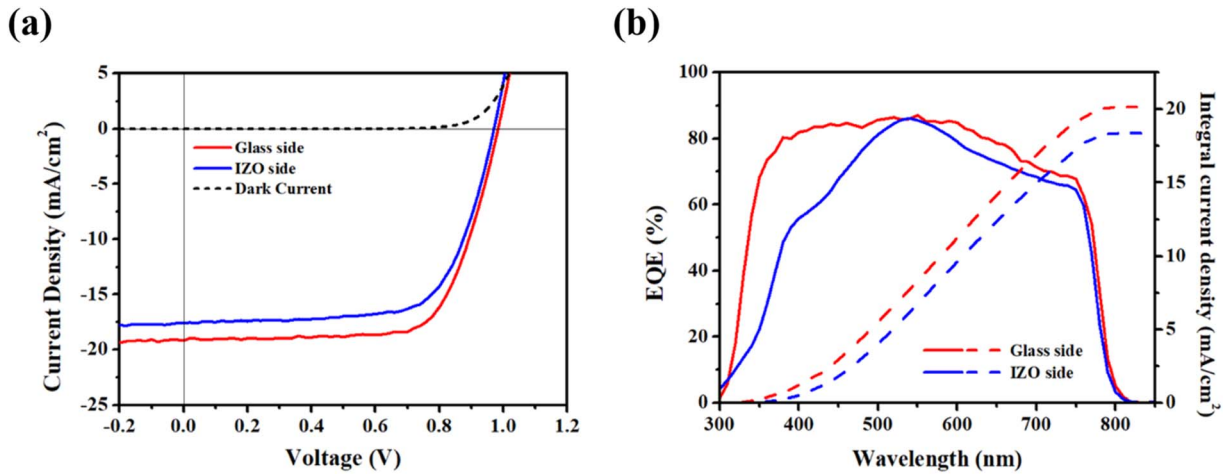

Fig. 7 (a) *J–V* curve and (b) EQE spectra of the bifacial device with 0.4 wt% PEIE under 1 sun illumination from glass and IZO sides.

Table 3 Photovoltaic characteristics of the bifacial device with 0.4 wt% PEIE under front and rear illumination

Illumination side	V_{oc} (V)	J_{sc} (mA cm^{-2})	FF (%)	PCE (%)	Bifacial factor
Front side (glass)	0.98	19.1	71.8	13.3	0.88
Rear side (IZO)	0.97	17.6	68.6	11.7	

sputtering of the first sputtering process, resulted in excessively high resistance of the IZO film. Thus, no significant enhancement in PV performance was achieved. The increased resistance observed when using soft sputtered IZO on ALD SnO_2 can be attributed to the poor film quality of IZO formed under low-energy deposition conditions. According to Thornton's structural zone model of sputtered films,[30] deposition under low sputtering power and low substrate temperature conditions leads to Zone 1-type growth, characterized by a porous and rough microstructure due to limited surface mobility of adatoms. This porous morphology reduces film density and increases electrical resistivity due to reduced grain connectivity and enhanced carrier scattering. Recent studies have further demonstrated that low-energy sputtered IZO films exhibit high sheet resistance and rough surfaces, particularly when deposited on dense underlayers like ALD-grown SnO_2.[31] Therefore, in our case, the soft IZO layer deposited at 10 W on top of compact ALD SnO_2 likely suffers from insufficient densification, resulting in high series resistance and degraded carrier transport. This suggests that while soft sputtering helps reduce ion damage, it may compromise the electrical performance due to poor IZO film quality.

To reduce the resistance of the IZO film, 1-step high-power sputtering deposition was further used to achieve the required transparent rear electrode. The results indicate that the devices deposited with a 10 nm SnO_2 buffer layer, under front illumination, achieved a V_{oc} of 0.96 V, a J_{sc} of 20.7 mA cm^{-2}, an FF of 71.2%, and a PCE of 14.4%. When the thickness of the ALD-prepared SnO_2 buffer layer increased to 20 nm, it also led to increased resistance, thereby reducing the J_{sc} and FF of the device and lowering the PCE to 13.1%. Hence, in ALD buffer layer preparation, an appropriate thickness is crucial to effectively mitigate damage during sputtering and maintain effective charge transport. Blindly increasing thickness would elevate device resistance and consequently degrade device performance. To optimize ALD-deposited SnO_2 buffer layers, we systematically tested devices with 5 nm, 10 nm, 15 nm, and 20 nm thicknesses. As shown in Fig. S2,† the 10 nm thickness yielded the best performance. The 5 nm layer was too thin to effectively protect the underlying layers, while increasing the thickness to 15 or 20 nm introduced higher series resistance and reduced carrier extraction, leading to lower PCE. Series resistance (R_s) values extracted from *J–V* fitting further confirm the trade-off between protection and charge transport. As shown in Table S1,† R_s decreased from 84.14 Ω (5 nm) to a minimum of 33.35 Ω (10 nm) and then increased to 50.26 Ω (15 nm) and 112.44 Ω (20 nm), supporting that both under- and over-thick SnO_2 layers compromise device performance. Under rear illumination, the efficiency was 12.1%, and the bifacial factor of the bifacial device is 0.84. The *J–V* curves and EQE spectra of the as-fabricated bifacial device under front and rear illumination are shown in Fig. 8. The corresponding PV parameters are provided in Table 4.

To further enhance device performance under rear illumination, 100 nm of MgF_2 was deposited on the IZO by evaporation to serve as an ARC layer.[32,33] The *J–V* curves and EQE spectra of the bifacial-illuminated PSCs under front and rear illumination are presented in Fig. 9(a) and (b), respectively. From the EQE spectra in Fig. 9(b), the deposition of the ARC MgF_2 layer significantly improves the device performance, especially increasing the J_{sc} to 20.2 mA cm^{-2} under rear illumination. The device efficiency under front illumination reached 16.2%, while under rear illumination, the efficiency was 15.4%. The bifacial factor of the bifacial device increased from 0.84–0.88 to 0.95 (Table 5).

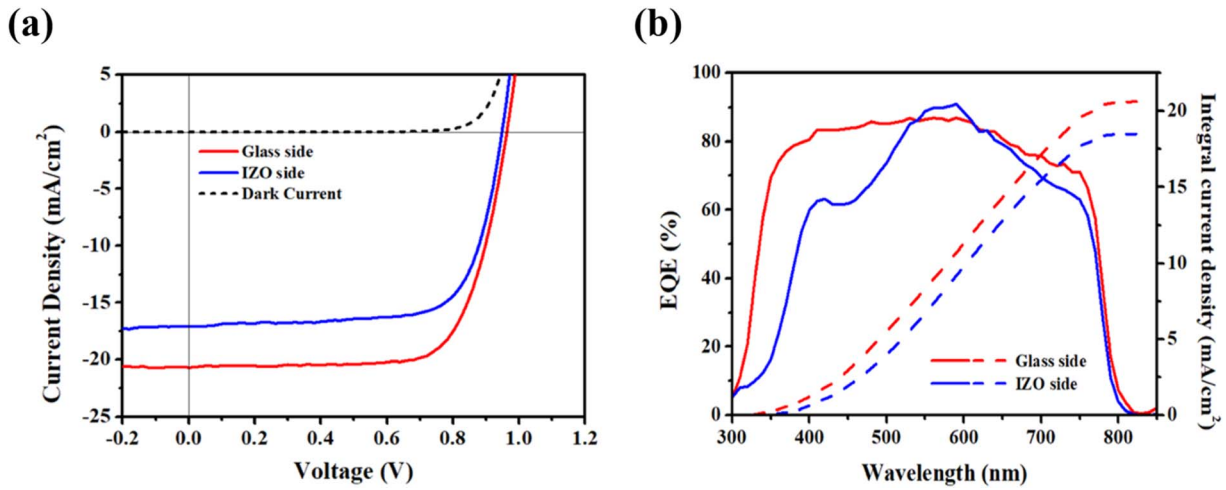

Fig. 8 (a) *J*–*V* curve and (b) EQE spectra of the ALD SnO_2 10 nm bifacial device under 1 sun illumination from glass and IZO sides.

Table 4 Photovoltaic characteristics of the ALD SnO_2 10 nm bifacial device under front and rear illumination

Illumination side	V_{oc} (V)	J_{sc} (mA cm^{-2})	FF (%)	PCE (%)	Bifacial factor
Front side (glass)	0.96	20.7	72.0	14.4	0.84
Rear side (IZO)	0.95	17.1	73.7	12.1	

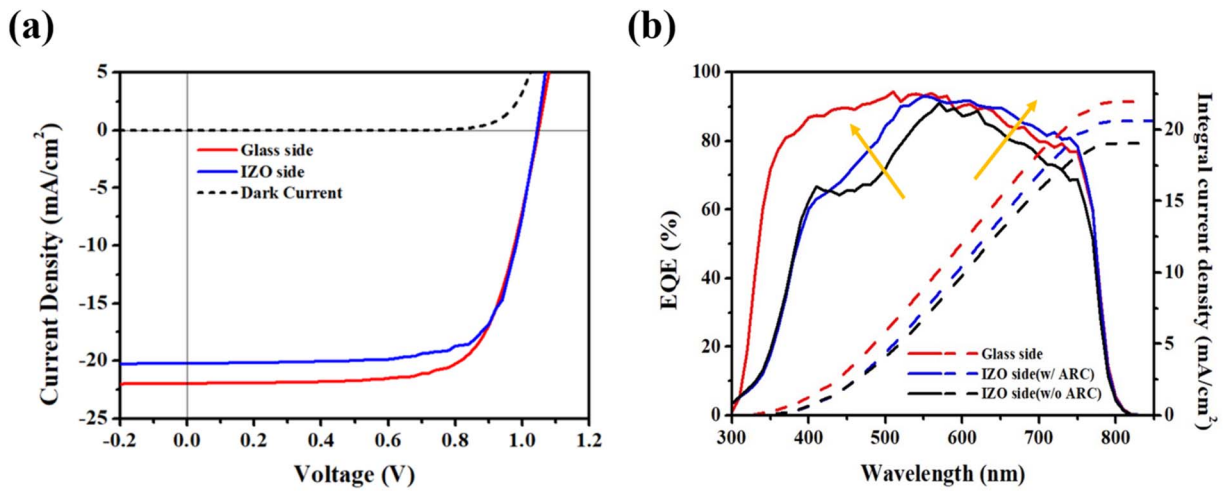

Fig. 9 (a) *J*–*V* curves and (b) EQE spectra of ALD SnO_2 bifacial device with an ARC illuminated with 1 sun from glass and IZO sides.

Table 5 Photovoltaic characteristics of the ALD SnO_2 bifacial device with an ARC under front and rear illumination

Illumination side	V_{oc} (V)	J_{sc} (mA cm^{-2})	FF (%)	PCE (%)	Bifacial factor
Front side (glass)	1.05	21.9	70.8	16.2	0.95
Rear side (IZO)	1.04	20.2	73.6	15.4	

2.5 Bifacial illumination measurements under different light intensity conditions

Bifacial illumination measurements under various incident light intensities were conducted for devices prepared with different buffer layer methods. This study explored whether bifacial PSCs could offer higher power output per unit area compared to monofacial PSCs. The front and rear PCEs and corresponding PV parameters of bifacial devices with different

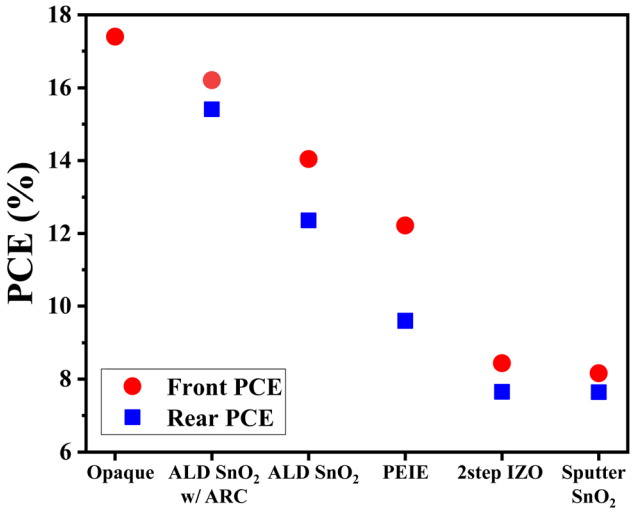

Fig. 10 PCE of the opaque device and bifacial devices with different buffer layers under 1 sun illumination from glass and IZO sides.

buffer layer preparation methods are compared with those of opaque devices in Fig. 10 and Table 6.

In the bifacial illumination measurement analysis, two solar simulators were used with different light intensities to simultaneously illuminate the bifacial device from both sides, as illustrated in Fig. 11. Three different measurement conditions were set:

Condition 1: the front side of the bifacial device was illuminated with a light intensity close to that of a clear sky (1 sun). Under this condition, the back-side illumination intensity was gradually increased from 0.2 sun to 1 sun.

Condition 2: the front side of the bifacial device was illuminated with a light intensity close to that of an overcast sky (0.6 sun). Under this condition, the back-side illumination intensity was gradually increased from 0.2 sun to 1 sun.

Condition 3: the front side of the bifacial device was illuminated with a light intensity close to that of an indoor environment or rainy day (0.2 sun). Under this condition, the back-side illumination intensity was gradually increased from 0.2 sun to 1 sun.

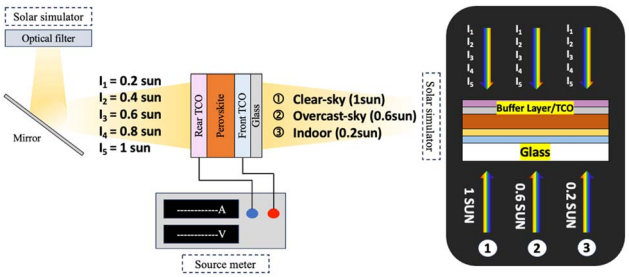

Fig. 11 Schematic measurement of bifacial illumination with simulated scenarios of clear sky, overcast sky, and indoor conditions.

2.6. Clear sky (1 sun)

Fig. 12(a) shows the power output of bifacial devices under AM 1.5 G one sun illumination from the glass substrate, with varying light illumination intensities from 0.2 to 1 sun from the IZO side. In the case of opaque devices, increasing the rear-side light intensity does not lead to an increase in the power generation. This is reasonable because opaque devices have a metallic rear electrode, which reflects any additional rear-side illumination, preventing it from reaching the perovskite absorption layer and generating additional power. On the other hand, for bifacial devices (regardless of the buffer used) under the same illumination scenario, as rear-side light intensity gradually increases, the power generation increases accordingly. For devices using the ALD SnO_2 buffer layer with an ARC, the power generation of the bifacial cell is comparable to that of the opaque device under 0.1 sun of additional back-side illumination. When rear-side illumination exceeds 0.1 sun, bifacial devices using the ALD SnO_2 buffer layer with an ARC begin to generate more power than single-sided opaque devices. Bifacial devices using the ALD SnO_2 buffer layer without an ARC exhibit less current gain at the back electrode compared to those with an ARC, requiring rear-side light intensity to exceed 0.4 sun for their power output to exceed that of opaque devices. Increased J_{sc} under rear illumination in MA-containing perovskite devices is primarily attributed to the presence of an ARC on the IZO side. The ARC reduces optical losses at the TCO interface and enhances light in-coupling, leading to greater photocarrier

Table 6 PV parameters and bifacial factor of the opaque device and bifacial devices with different buffer layers under 1 sun illumination from glass and IZO sides

Devices	Illumination side	V_{oc} (V)	J_{sc} (mA cm^{-2})	FF (%)	PCE (%)	Bifacial factor
Opaque	Glass	1.06	21.8	75.4	17.4	—
	IZO	—	—	—	—	
ALD SnO_2 with an ARC	Glass	1.05	21.9	70.8	16.2	0.95
	IZO	1.04	20.2	73.6	15.4	
ALD SnO_2	Glass	0.99	19.9	71.4	14.0	0.88
	IZO	0.97	17.6	71.3	12.4	
PEIE	Glass	0.95	20.5	62.6	12.2	0.79
	IZO	0.96	15.7	65.3	9.6	
2-step sputtered IZO	Glass	0.91	17.8	51.7	8.4	0.91
	IZO	0.95	15.0	52.9	7.6	
Sputtered SnO_2	Glass	0.88	20.0	46.1	8.2	0.93
	IZO	0.89	17.7	48.5	7.6	

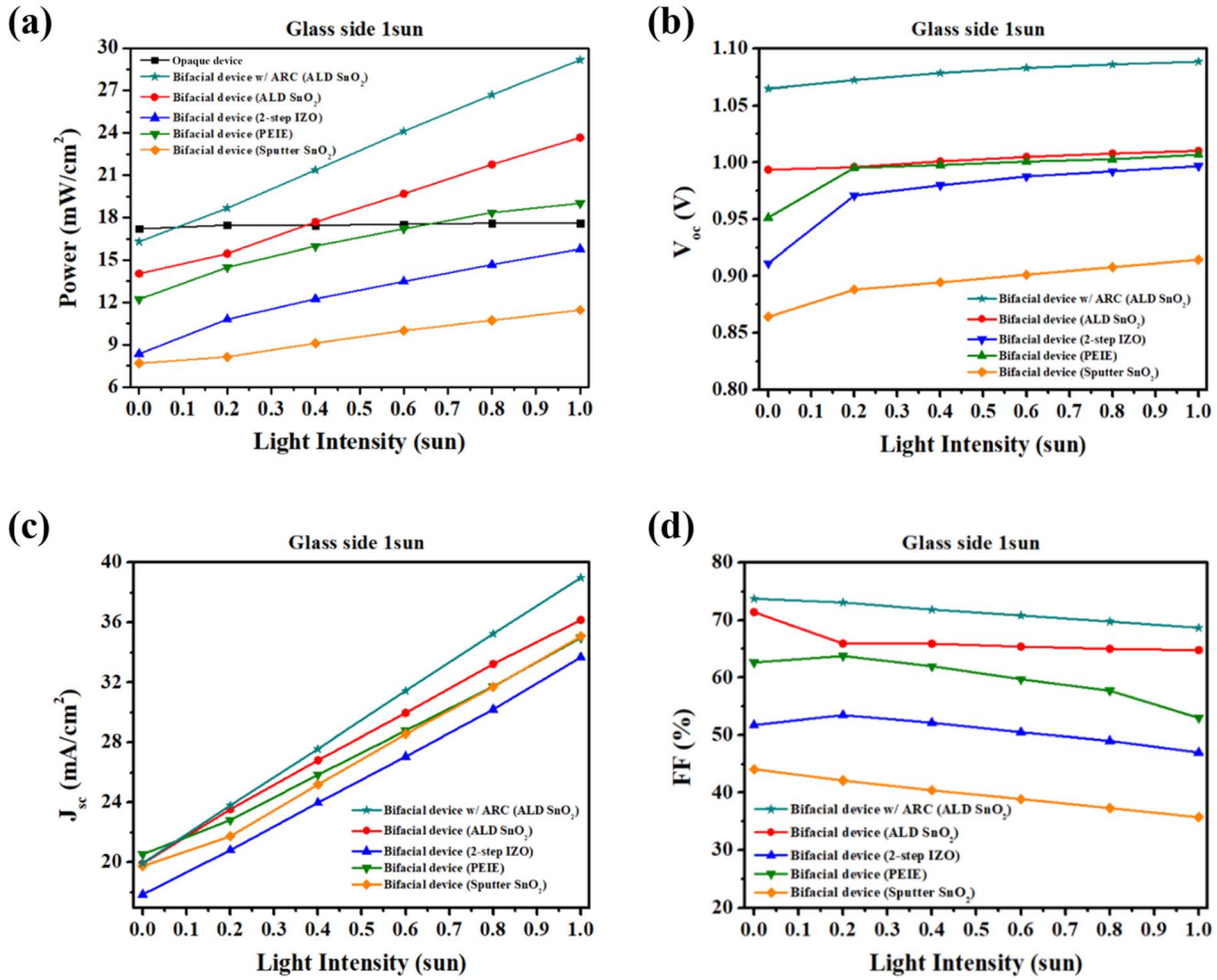

Fig. 12 (a) Power output density, (b) V_{OC}, (c) J_{SC}, and (d) FF of different bifacial devices under fixed 1 sun illumination on the glass side (approaching sunny day intensity) with varying light intensities from the IZO side.

generation from the rear side. This, combined with favorable optical absorption properties of the MA-containing perovskite, explains the sharp J_{sc} enhancement with increasing rear-side light intensity.

As the buffer layer's resistance to bombardment decreases, the threshold of light intensity for the bifacial cell to outperform the opaque device increases. Spin-coated PEIE bifacial devices achieve higher power output than single-sided opaque devices when rear-side light intensity is approximately 0.7 sun. On the other hand, bifacial devices with 2-step IZO and sputtered SnO_2 layers suffer from interface damage during sputtering, resulting in significant defects that impair carrier transport, and hence, their power output remains lower than that of opaque devices (Fig. 12(a)). As a result, the power generation of this bifacial cell will not surpass that generated from the opaque device even at 1 sun of back-side illumination. The major gain in power generation is contributed by the enhanced current density due to back-side illumination, as seen in Fig. 12(b–d). The increase in J_{sc} with increasing light intensity is linear, and the V_{oc} increase is proportional to the logarithm of incoming light intensity. Moreover, the decrease in the FF is attributed to the higher resistivity of IZO compared to metals, which increases the resistive loss as the total current increases in the device upon additional back-side illumination (Fig. 12(d)).[34]

2.7. Overcast sky (0.6 sun)

For opaque devices illuminated with 0.6 sun, the power output decreases from 18 mW cm^{-2} to 10 mW cm^{-2} due to the reduced front illumination. Bifacial ALD SnO_2 devices without an ARC, which required 0.4 sun rear illumination to exceed the power output of opaque devices under clear sky conditions (1 sun), only need about 0.2 sun rear illumination under overcast conditions to exceed the power output of single-sided opaque devices. Bifacial devices with an ARC require only 0.1 sun rear illumination to exceed the power output of opaque devices. Bifacial devices with spin-coated PEIE require only 0.3 sun of rear-side illumination, reduced from the previous 0.7 sun, to exceed the power output of monofacial opaque devices. As the front-side illumination intensity weakens, the threshold for bifacial devices to gain more power output shifts to a lower backside illumination intensity (Fig. 13(a)).

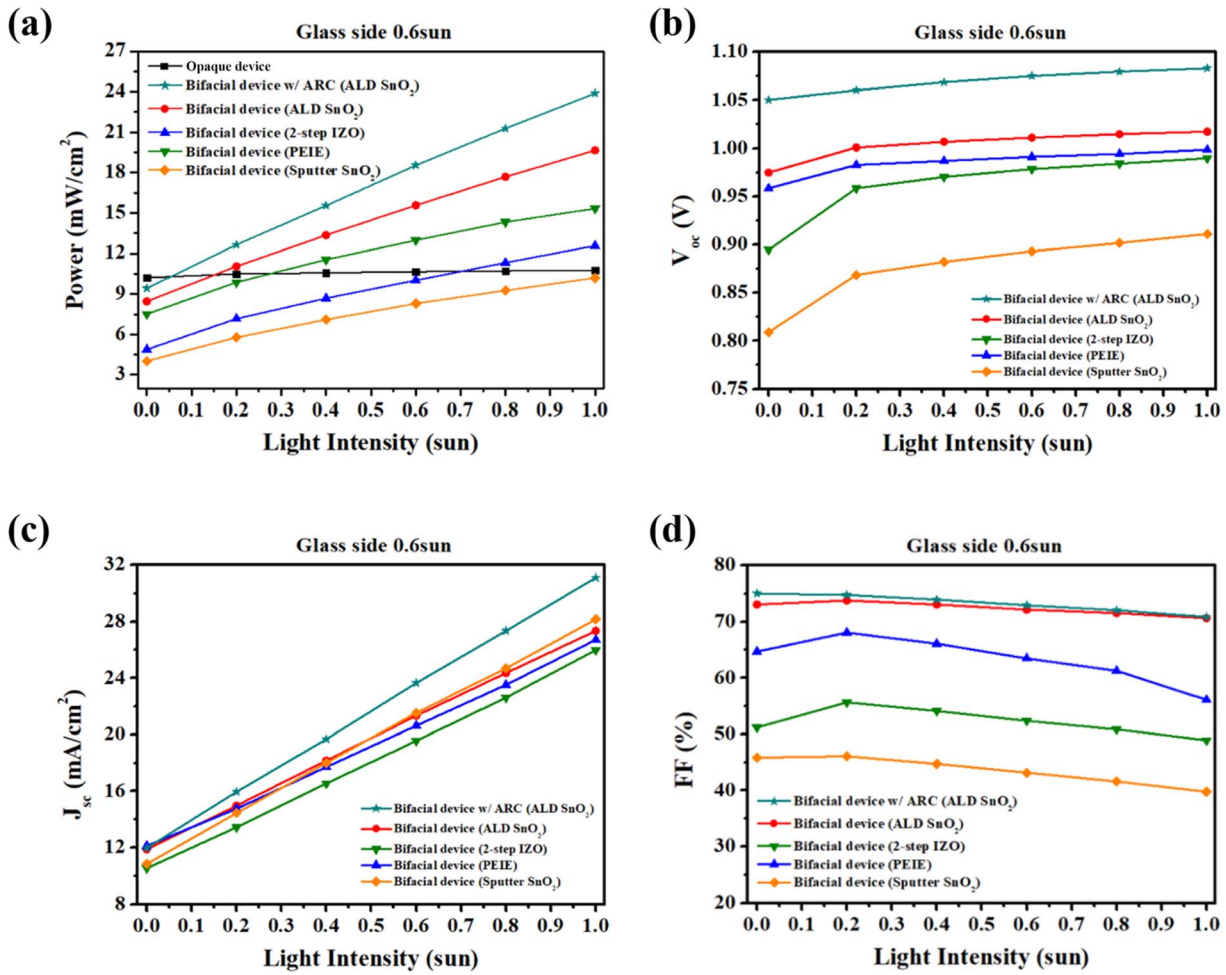

Fig. 13 (a) Power output density, (b) V_{oc}, (c) J_{sc}, and (d) FF of different bifacial devices under fixed 0.6 sun illumination on the glass side (approaching cloudy day intensity) with varying light intensities from the IZO side.

2.8. Indoor or rainy day (0.2 sun)

For scenarios with low-intensity front-side illumination, bifacial devices generate significantly more power when additional back-side illumination is applied. The power output of bifacial devices with ALD SnO_2 and spin-coated PEIE exceeds that of opaque devices with less than 0.1 sun of back-side illumination (Fig. 14(a)). Bifacial devices with 2-step IZO and sputtered SnO_2 also exceed the power output of opaque devices with 0.2 sun of back-side illumination (Fig. 14(a)). For the 2-step IZO and sputtered SnO_2 bifacial devices, the threshold of back-side illumination intensity to generate more power than the opaque device significantly decreased to 0.2 sun. Meanwhile, under weaker rear-side illumination (<0.4 sun), the power output of bifacial devices with spin-coated PEIE surpasses that of bifacial ALD SnO_2 devices without an ARC. This is likely because low light intensity conditions are more tolerant to defects, allowing bifacial devices with interfacial damage to perform well under low light intensity. It is interesting to see that the 2-step IZO and sputtered SnO_2 bifacial devices, which do not gain more power generation under bifacial illumination at 1 sun front-side illumination, can deliver additional power under low light conditions. This suggests the beneficial effects of using bifacial cells for indoor or Internet of Things (IOT) applications.

To further optimize the bifacial cell performances, we applied a p-i-n structure with FTO/SAM/$FA_{0.78}Cs_{0.22}Pb(I_{0.85}Br_{0.15})_3$/$C_{60}$/ALD SnO_2/IZO/Ag architecture with an MA free perovskite. The change in the SAM from Me-4PACz to 3PATAT-C3 was driven by its good coverage and better overlap for perovskite. We added the performance comparison between Me-4PACz and 3PATAT-C3 in ESI Fig. S3,† where both SAMs almost showed similar performance, but the device coverage was better in the 3PATAT-C3 SAM. Their *J*–*V* and IPCE are illustrated in Fig. 15 with their photovoltaic parameters in Table 7. We further conducted bifacial illumination for this MA free device, where their power output, J_{sc}, V_{oc} and FF are shown in Fig. 16.

The *J*–*V* characteristics in Fig. 15(a) show the photovoltaic behavior under front and rear illumination, where the front-side (glass-side) illumination exhibited a higher current density compared to the rear-side (IZO-side) illumination. The IPCE spectra in Fig. 15(b) further reveal the device's spectral response, demonstrating efficient charge collection across the visible range, with a slightly reduced response at short (350–500

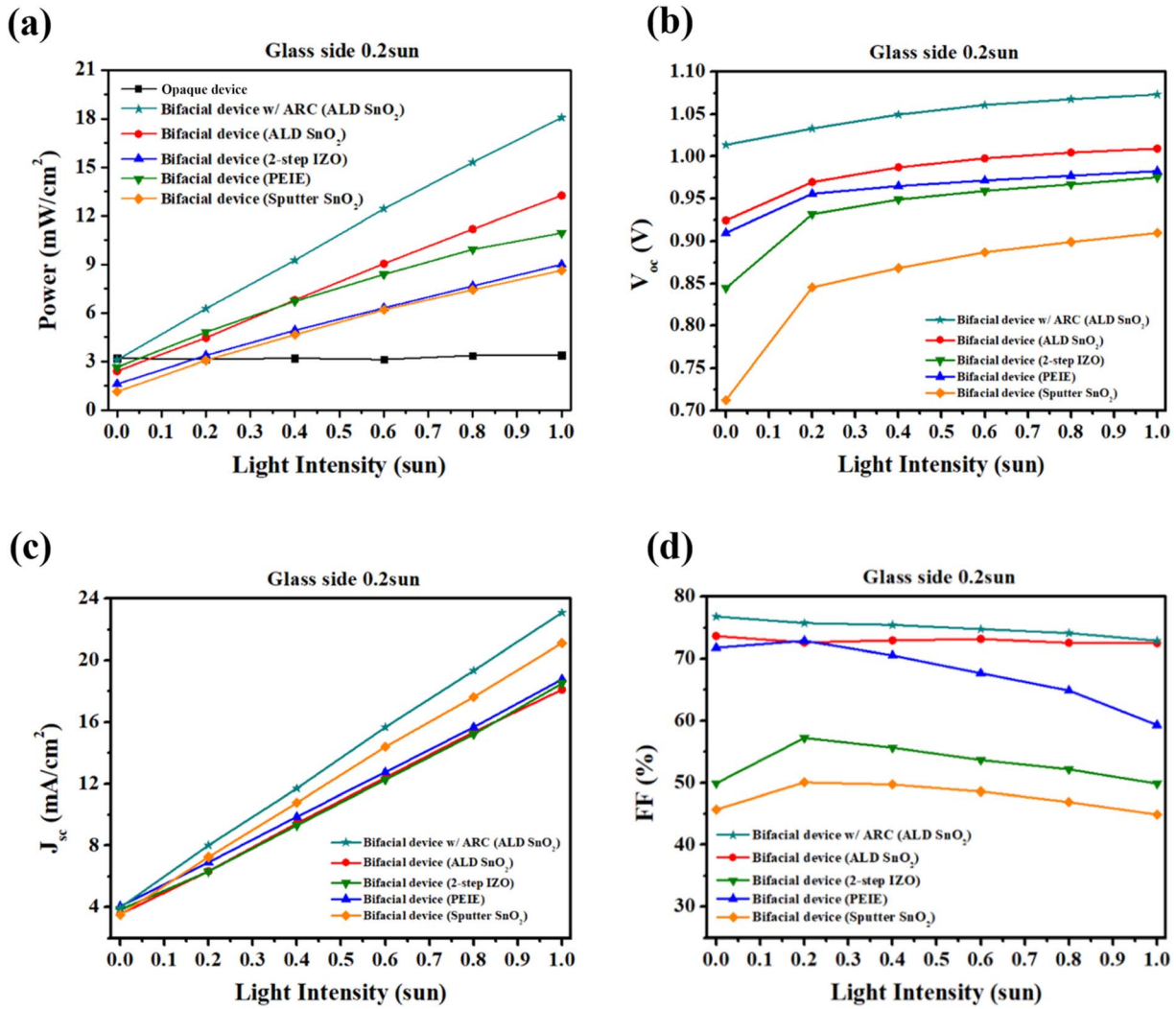

Fig. 14 (a) Power output density, (b) V_{oc}, (c) J_{sc}, and (d) FF of different bifacial devices under fixed 0.2 sun illumination on the glass side (approaching rainy day intensity) with varying light intensities from the IZO side.

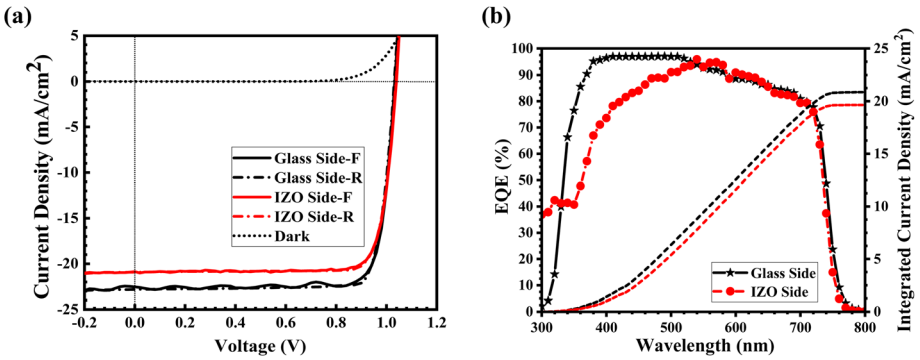

Fig. 15 (a) J–V curve and (b) EQE spectra of the MA free perovskite ($FA_{0.78}Cs_{0.22}Pb(I_{0.85}Br_{0.15})_3$) bifacial device under 1 sun illumination from glass and IZO sides.

nm) wavelengths for rear-side illumination. Fig. 16 presents the power output, J_{sc}, V_{oc}, and fill factor (FF) as a function of rear-side light intensity. The power output (Fig. 16(a)) increases with light intensity for both illumination conditions, with the front-side illumination showing slightly higher values. The open-circuit voltage (V_{oc}) (Fig. 16(b)) remains relatively stable, with only minor variations, indicating that charge recombination mechanisms are similar for both illumination conditions.

Table 7 PV parameters and bifacial factor of MA-Free perovskite bifacial devices

Illumination side	Scan	V_{oc} (V)	J_{sc} (mA cm^{-2})	FF (%)	PCE (%)	Bi-facial factor
Glass side	Forward	1.03	22.5	83.4	19.3	91.32
	Reverse	1.03	22.8	84.6	19.7	
IZO side	Forward	1.03	20.9	82.8	17.9	
	Reverse	1.03	20.8	84.2	18.0	

The short-circuit current (J_{sc}) (Fig. 16(c)) follows a linear trend, reflecting the expected photocurrent generation under varying light intensities. However, the FF (Fig. 16(d)) exhibits a slight reduction with the rear-side illumination, suggesting some resistive or interfacial losses when light is incident from the IZO side.

Under standard front-side illumination (glass side), the device exhibited a short-circuit current density (J_{sc}) of 22.8 mA cm^{-2} in forward scan, while under rear-side illumination (IZO side), the J_{sc} was 20.8 mA cm^{-2}. The bi-faciality factor, which quantifies the efficiency of the rear-side response compared to the front, was calculated to be 91.32%, indicating excellent bifacial performance. The observed minimal J_{sc} increase in MA-free devices under low IZO-side illumination may be due to the absence of the ARC and increased interfacial recombination. The power output and FF showed a slight decrease under rear illumination, suggesting minor optical and recombination losses. Notably, no anti-reflective coating (ARC) was applied to the IZO side, which could have contributed to the lower J_{sc} for rear illumination. The addition of an ARC could potentially enhance

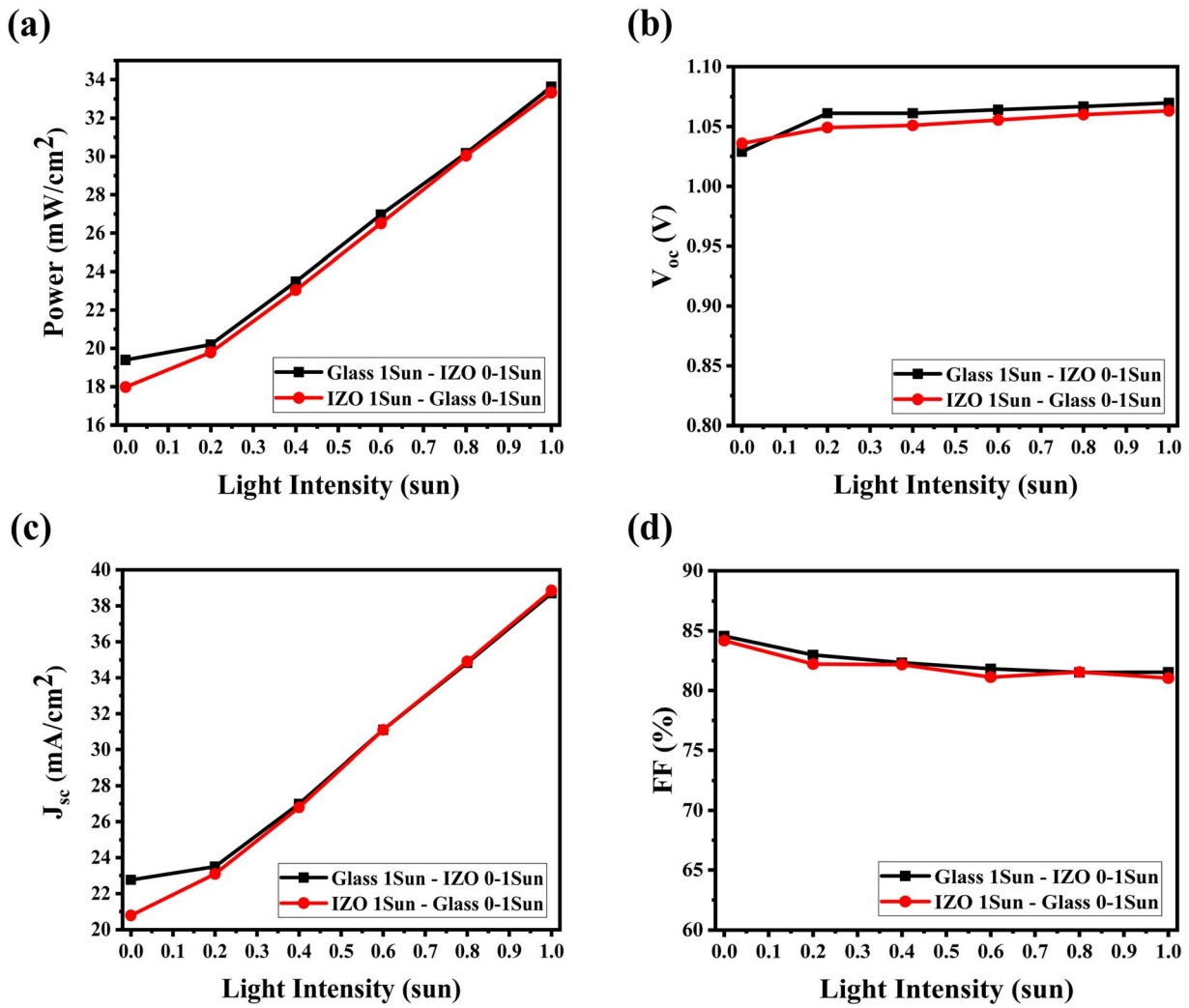

Fig. 16 (a) Power output and (b) V_{oc} (c) photocurrent and (d) FF of the MA free perovskite ($FA_{0.78}Cs_{0.22}Pb(I_{0.85}Br_{0.15})_3$) bifacial illuminated device as a function of backside illumination intensities with fixed 1 sun intensity from glass (blackline) and IZO (red line) sides.

light absorption at the rear interface, further improving the photocurrent and overall bifacial efficiency of the device.

3. Conclusion

The resistance of the buffer layer against bombardment is crucial for the performance of bifacial devices. However, when using sputtering to prepare the buffer layer, even under extreme deposition parameter control, high-energy particles during the sputtering process still damage the interface, thereby deteriorating the device's performance. ALD offers excellent film coverage and precise thickness control, making it an effective candidate for preparing buffer layers to avoid sputtering damage. In this study, bifacial devices with buffer layers prepared by ALD and anti-reflection coating achieved the highest front illumination efficiency of 16.2% and rear illumination efficiency of 15.4%, resulting in a bifacial factor of 0.95. The bifacial illumination measurements under specific working conditions were implemented. Under simulated clear sky (1 sun) illumination, bifacial devices with ALD SnO_2 and spin-coated PEIE showed higher power output per unit area compared to single-sided opaque devices when the back-side illumination was 0.1 sun (with an ARC), 0.4 sun (ALD), and 0.7 sun (PEIE). This demonstrates that bifacial devices can indeed produce more energy than opaque monofacial devices. Additionally, as the simulated light intensity in the environment decreases (such as overcast (0.6 sun) or indoor (0.2 sun)), the requirement for the buffer layer' resistance to bombardment is reduced. Under low light conditions, even bifacial devices with 2-step IZO and sputtered SnO_2 can exceed the power generation of opaque devices, achieving the expected bifacial benefits. As a result, appropriate buffer layer preparation methods can be applied for different working conditions to fulfill economic benefits.

For high-performance MA-free perovskite bifacial solar cell in a p-i-n architecture with the composition $FA_{0.78}Cs_{0.22}Pb(I_{0.85}Br_{0.15})_3$, the device exhibited excellent bifacial characteristics, achieving a bifacial factor of 91.32%, with a front-side (glass-side) short-circuit current density (J_{sc}) of 22.8 mA cm^{-2} and a rear-side (IZO-side) J_{sc} of 20.8 mA cm^{-2}. The power output, open-circuit voltage, and fill factor remained stable across different light intensities, indicating good operational reliability under bifacial conditions. The efficiency drop in rear-side illumination was attributed to minor optical and interfacial losses, which could potentially be mitigated by incorporating an anti-reflective coating (ARC) on the IZO layer to enhance light absorption and improve photocurrent generation. These results highlight the potential of MA-free perovskite bifacial solar cells for high-efficiency and stable energy conversion, paving the way for further optimization in tandem and large-area photovoltaic applications.

Data availability

Data for this article are available at the NCKU Thesis Service of National Cheng Kung University at **https://www.lib.ncku.edu.tw/service/inhouse/thesis_en.php**

Conflicts of interest

There are no conflicts to declare.

Acknowledgements

The authors gratefully acknowledge financial support from the National Science and Technology Council of Taiwan (NSTC 113-2223-E-006-011) and (NSTC 113-2622-8-006-022). This work was financially supported by the Hierarchical Green-Energy Materials (HiGEM) Research Center, from the Featured Areas Research Center Program within the framework of the Higher Education Sprout Project by the Ministry of Education (MOE) in Taiwan. This research was supported in part by the Higher Education Sprout Project, Ministry of Education to the Headquarter of University Advancement at National Cheng Kung University (NCKU). This research is financially supported by the Academia Sinica Net-Zero Technology Research and Development Program (AS-KPQ-113-NETZ-05).

References

1 Z. Song, *et al.*, Perovskite Solar Cells Go Bifacial—Mutual Benefits for Efficiency and Durability, *Adv. Mater.*, 2022, **34**(4), 2106805.
2 P. Kumar, G. Shankar and B. Pradhan, Recent progress in bifacial perovskite solar cells, *Appl. Phys. A*, 2022, **129**(1), 63.
3 E. Aydin, *et al.*, Sputtered transparent electrodes for optoelectronic devices: Induced damage and mitigation strategies, *Matter*, 2021, **4**(11), 3549–3584.
4 Q. Jiang, *et al.*, Highly efficient bifacial single-junction perovskite solar cells, *Joule*, 2023, **7**(7), 1543–1555.
5 Z. Song, *et al.*, Assessing the true power of bifacial perovskite solar cells under concurrent bifacial illumination, *Sustain. Energy Fuels*, 2021, **5**(11), 2865–2870.
6 H. Hao, *et al.*, Energy Yield Prediction of Bifacial Perovskite/Silicon Tandem Photovoltaic Modules, *Sol. RRL*, 2023, **7**(15), 2300218.
7 NREL, Best Research-Cell Efficiency Chart. **https://www.nrel.gov/pv/cell-efficiency.html**, (accessed 2024).
8 J. Y. Kim, *et al.*, High-Efficiency Perovskite Solar Cells, *Chem. Rev.*, 2020, **120**(15), 7867–7918.
9 I. Mathews, *et al.*, Economically Sustainable Growth of Perovskite Photovoltaics Manufacturing, *Joule*, 2020, **4**(4), 822–839.
10 F. H. Isikgor, *et al.*, Molecular engineering of contact interfaces for high-performance perovskite solar cells, *Nat. Rev. Mater.*, 2023, **8**(2), 89–108.
11 Q. Jiang, *et al.*, Surface reaction for efficient and stable inverted perovskite solar cells, *Nature*, 2022, **611**(7935), 278–283.
12 R. Lin, *et al.*, All-perovskite tandem solar cells with improved grain surface passivation, *Nature*, 2022, **603**(7899), 73–78.
13 K. Ellmer, Past achievements and future challenges in the development of optically transparent electrodes, *Nat. Photonics*, 2012, **6**(12), 809–817.

14 S. D. H. Naqvi, *et al.*, Mitigating Intrinsic Interfacial Degradation in Semi-Transparent Perovskite Solar Cells for High Efficiency and Long-Term Stability, *Adv. Energy Mater.*, 2023, **13**(47), 2302147.
15 K. O. Brinkmann, *et al.*, Suppressed decomposition of organometal halide perovskites by impermeable electron-extraction layers in inverted solar cells, *Nat. Commun.*, 2017, **8**(1), 13938.
16 K. A. Bush, *et al.*, Thermal and Environmental Stability of Semi-Transparent Perovskite Solar Cells for Tandems Enabled by a Solution-Processed Nanoparticle Buffer Layer and Sputtered ITO Electrode, *Adv. Mater.*, 2016, **28**(20), 3937–3943.
17 T. Welzel and K. Ellmer, Negative ions in reactive magnetron sputtering, *Vakuum Forsch. Praxis*, 2013, **25**(2), 52–56.
18 T. Welzel and K. Ellmer, Negative oxygen ion formation in reactive magnetron sputtering processes for transparent conductive oxides, *J. Vac. Sci. Technol. A*, 2012, **30**(6), 061306.
19 K. Ellmer and T. Welzel, Reactive magnetron sputtering of transparent conductive oxide thin films: Role of energetic particle (ion) bombardment, *J. Mater. Res.*, 2012, **27**(5), 765–779.
20 M. Härtel, *et al.*, Reducing sputter damage-induced recombination losses during deposition of the transparent front-electrode for monolithic perovskite/silicon tandem solar cells, *Sol. Energy Mater. Sol. Cells*, 2023, **252**, 112180.
21 J. Werner, *et al.*, Sputtered rear electrode with broadband transparency for perovskite solar cells, *Sol. Energy Mater. Sol. Cells*, 2015, **141**, 407–413.
22 H. Kanda, *et al.*, Analysis of Sputtering Damage on *I–V* Curves for Perovskite Solar Cells and Simulation with Reversed Diode Model, *J. Phys. Chem. C*, 2016, **120**(50), 28441–28447.
23 L. Xiong, *et al.*, Review on the Application of SnO_2 in Perovskite Solar Cells, *Adv. Funct. Mater.*, 2018, **28**(35), 1802757.
24 M. Kam, *et al.*, Room-Temperature Sputtered SnO_2 as Robust Electron Transport Layer for Air-Stable and Efficient Perovskite Solar Cells on Rigid and Flexible Substrates, *Sci. Rep.*, 2019, **9**(1), 6963.
25 D. Kim, *et al.*, Efficient, stable silicon tandem cells enabled by anion-engineered wide-bandgap perovskites, *Science*, 2020, **368**(6487), 155–160.
26 N. Ren, *et al.*, 50 °C low-temperature ALD SnO_2 driven by H_2O_2 for efficient perovskite and perovskite/silicon tandem solar cells, *Appl. Phys. Lett.*, 2022, **121**(3), 033502.
27 V. Zardetto, *et al.*, Atomic layer deposition for perovskite solar cells: research status, opportunities and challenges, *Sustain. Energy Fuels*, 2017, **1**(1), 30–55.
28 B. Chen, *et al.*, Insights into the Development of Monolithic Perovskite/Silicon Tandem Solar Cells, *Adv. Energy Mater.*, 2022, **12**(4), 2003628.
29 A. J. Bett, *et al.*, Semi-Transparent Perovskite Solar Cells with ITO Directly Sputtered on Spiro-OMeTAD for Tandem Applications, *ACS Appl. Mater. Interfaces*, 2019, **11**(49), 45796–45804.
30 J. A. Thornton, Influence of apparatus geometry and deposition conditions on the structure and topography of thick sputtered coatings, *J. Vac. Sci. Technol.*, 1974, **11**(4), 666–670.
31 K. Liu, *et al.*, Reducing sputter induced stress and damage for efficient perovskite/silicon tandem solar cells, *J. Mater. Chem. A*, 2022, **10**(3), 1343–1349.
32 N. Rodkey, *et al.*, Efficient Micrometer Thick Bifacial Perovskite Solar Cells, *Adv. Energy Mater.*, 2024, **14**(21), 2400058.
33 S.-K. Jung, *et al.*, Effects of MgF_2 anti-reflection coating on optical losses in metal halide perovskite solar cells, *Nanotechnology*, 2024, **35**(13), 135401.
34 D. Kiermasch, *et al.*, Effects of Masking on Open-Circuit Voltage and Fill Factor in Solar Cells, *Joule*, 2019, **3**(1), 16–26.